AIP | Physics of Plasmas

Direct Vlasov simulations of electron-attracting cylindrical Langmuir probes in flowing plasmas

G. Sánchez-Arriaga and D. Pastor-Moreno

Citation: Physics of Plasmas (1994-present) **21**, 073504 (2014); doi: 10.1063/1.4889732
View online: http://dx.doi.org/10.1063/1.4889732
View Table of Contents: http://scitation.aip.org/content/aip/journal/pop/21/7?ver=pdfcov
Published by the AIP Publishing

Direct Vlasov simulations of electron-attracting cylindrical Langmuir probes in flowing plasmas

G. Sánchez-Arriaga and D. Pastor-Moreno
Departamento de Física Aplicada, Escuela Técnica Superior de Ingenieros Aeronáuticos, Universidad Politécnica de Madrid, Plaza de Cardenal Cisneros 3, 28040 Madrid, Spain

(Received 15 April 2014; accepted 24 June 2014; published online 10 July 2014)

Current collection by positively polarized cylindrical Langmuir probes immersed in flowing plasmas is analyzed using a non-stationary direct Vlasov-Poisson code. A detailed description of plasma density spatial structure as a function of the probe-to-plasma relative velocity U is presented. Within the considered parametric domain, the well-known electron density maximum close to the probe is weakly affected by U. However, in the probe wake side, the electron density minimum becomes deeper as U increases and a rarified plasma region appears. Sheath radius is larger at the wake than at the front side. Electron and ion distribution functions show specific features that are the signature of probe motion. In particular, the ion distribution function at the probe front side exhibits a filament with positive radial velocity. It corresponds to a population of rammed ions that were reflected by the electric field close to the positively biased probe. Numerical simulations reveal that two populations of trapped electrons exist: one orbiting around the probe and the other with trajectories confined at the probe front side. The latter helps to neutralize the reflected ions, thus explaining a paradox in past probe theory. © *2014 AIP Publishing LLC*.
[http://dx.doi.org/10.1063/1.4889732]

I. INTRODUCTION

Plasma structure in the neighborhood of material walls is a fundamental problem in plasma physics. Theoretical models were developed during almost one century and used in relevant technological applications. Two examples are Langmuir probes,[1] which are routinely used for plasma diagnostic and bare electrodynamic tethers,[2] that can be used to deorbit satellites at the end of life and mitigate the space debris problem. The steady-state properties of plasma sheaths in non-flowing plasma are now well understood.[1,3–7] In flowing plasmas, both analytical works in particular regimes[1,8–10] and numerical simulations of the Vlasov-Poisson system[11–14] were carried out. Some issues, however, remain open.

An interesting paradox arises for cylindrical Langmuir probes positively polarized within the so called mesothermal regime;[15] i.e., probe velocity small (large) compared with electron (ion) thermal velocity. The faraway electron population would still be (nearly) isotropic and an important and very general result by Laframboise and Parker applies:[16] electron density N_e is less that the unperturbed plasma density N_0 everywhere. This result is valid even if the electric potential depends on the azimuthal angle θ, as it happens in the case of flowing plasmas. On the other hand, since probe bias is positive and ions are repelled, the hypersonic ion flow will result in an ion density N_i exceeding N_0 in a broad region at the probe front side. This would break the quasineutrality in a region much larger than the Debye length.

The explanation of the paradox may come from the violation of (at least) one of the hypothesis used in Ref. 16 to find the condition $N_e/N_0 < 1$. Besides the isotropic character of the electron distribution function, Ref. 16 assumed that (i) plasma reached an steady state and (ii) that there are no trapped particles. Violation of hypothesis (i) was invoked in Ref. 17, where plasma oscillations were detected in laboratory experiments. Possible electron trapping in energy troughs due to collisional effects was discussed in Ref. 3. However, since collisional trapping rate can be very small,[6] a non-stationary process called adiabatic trapping[18] has been proposed in Ref. 15 to explain the paradox. As electron potential wells develop in time, some electrons become trapped adiabatically. The *adiabatic* term comes from the fact that time variations in the electric potential, which are controlled by the ions, are very slow as compared with the motion of the electrons.

The confirmation of electron trapping at the front side cannot be carried out with stationary Vlasov-Poisson solvers[11,12,14] because they explicitly neglect this particle population. The computation of trapped particles requires a non-stationary Vlasov-Poisson solver, like the particle-in-cell (PIC) codes used to study Langmuir probes in the past.[13,19,20] However, PIC codes do not give an accurate representation when the number of particles per cell is small and they also introduce numerical noise. An alternative is the implementation of Eulerian or direct Vlasov codes. Unlike PIC codes, which use macro-particles to discretize Vlasov equation, direct Vlasov codes make a discretization of the distribution functions in both real and velocity space. The result is a code free of numerical noise but expensive from a computational point of view.

This work used numerical simulations to confirm that electron trapping at the probe front side occurs. Section II shows the modification carried out in the direct Vlasov code named Kilaps (Kinetic Langmuir probe software)[21] to

incorporate the probe-to-plasma relative motion. In Sec. III, the time evolution of the macroscopic variables, including collected current, is discussed. Sections IV and V describe the structure of the particle densities and distribution functions. The signatures of the probe motion in plasma variables are highlighted. In Sec. VI, two populations of trapped electrons, one of them at the probe front side, are shown. Discussion of results and comparisons with previous works are presented in Sec. VII.

II. MATHEMATICAL MODEL AND NUMERICAL ALGORITHM

A perfectly absorbing cylindrical probe of radius R and bias $\Phi_p(t)$ is moving with velocity $U(t)$ inside a collisionless, non-magnetized, Maxwellian plasma made of electrons an single-charged ions. Faraway from the probe, plasma density is equal to N_0, and electrons' and ions' temperatures are T_e and T_i, respectively. Cylindrical coordinates (r, θ), with origin at the center of the probe and angle $\theta = 0$ ($\theta = \pi$) corresponding to the wake (front or ram) side, are used. Time, position, and velocity vectors, electric potential, particles distribution functions, and densities are normalized as

$$\omega_{pe}t \to t, \quad \frac{r}{\lambda_{De}} \to r, \quad \frac{v}{\sqrt{kT_e/m_e}} \to v, \quad \frac{e\Phi}{kT_e} \to \Phi, \quad \frac{kT_e f_\alpha}{N_0 m_e} \to f_\alpha, \quad \frac{N_\alpha}{N_0} \to N_\alpha, \tag{1}$$

where the subscript $\alpha = e$ and i denotes electrons and ions. We also introduce the following dimensionless parameters and variables:

$$\rho \equiv \frac{R}{\lambda_{De}}, \quad \mu_\alpha \equiv \frac{m_\alpha}{m_e}, \quad \delta_\alpha \equiv \frac{T_\alpha}{T_e}, \quad \phi_p(t) \equiv \frac{e\Phi_p(t)}{kT_e}, \quad S(t) \equiv \frac{U(t)}{\sqrt{kT_i/m_i}}. \tag{2}$$

Using this normalization, Vlasov-Poisson system in cylindrical coordinates reads

$$\frac{\partial f_\alpha}{\partial t} + v_r\frac{\partial f_\alpha}{\partial r} + \frac{v_\theta}{r}\frac{\partial f_\alpha}{\partial \theta} + \left(\frac{v_\theta^2}{r} - \frac{\epsilon_\alpha}{\mu_\alpha}\frac{\partial \Phi}{\partial r}\right)\frac{\partial f_\alpha}{\partial v_r} - \frac{1}{r}\left(v_r v_\theta + \frac{\epsilon_\alpha}{\mu_\alpha}\frac{\partial \Phi}{\partial \theta}\right)\frac{\partial f_\alpha}{\partial v_\theta} = 0, \tag{3a}$$

$$\frac{\partial^2 \Phi}{\partial r^2} + \frac{1}{r}\frac{\partial \Phi}{\partial r} + \frac{1}{r^2}\frac{\partial^2 \Phi}{\partial \theta^2} = N_e - N_i, \tag{3b}$$

where $\epsilon_e = -1$, $\epsilon_i = 1$ and

$$N_\alpha(t, r, \theta) = \int\int f_\alpha(t, r, \theta, v_r, v_\theta) dv_r dv_\theta. \tag{4}$$

The boundary conditions of the problem are

$$f_\alpha(t, r = \rho, \theta, v_r > 0, v_\theta) = 0, \tag{5a}$$

$$f_\alpha(t, r \to \infty, \theta, v_r, v_\theta) = \frac{\mu_\alpha}{2\pi\delta_\alpha}\exp\left\{-\frac{\mu_\alpha}{2\delta_\alpha}\left[v_r^2 + v_\theta^2 + \frac{\delta_i}{\mu_i}S^2 - 2S\sqrt{\frac{\delta_i}{\mu_i}}(v_r\cos\theta - v_\theta\sin\theta)\right]\right\}, \tag{5b}$$

$$\Phi(t, r = \rho, \theta) = \phi_p(t), \quad \Phi(t, r \to \infty, \theta) \to 0. \tag{5c}$$

Boundary condition (5a) imposes that no particle is emitted by the probe. Faraway from the probe, a drifting Maxwellian is assumed (see Eq. (5b)).

Given initial conditions, $\Phi(0, r, \theta)$ and $f_\alpha(0, r, \theta, v_r, v_\theta)$, and laws $\phi_p(t)$ and $S(t)$, Sys. 3 is integrated with *Kilaps*, which is a modification of the code presented in Ref. 21. It implements a finite-difference method combined with an explicit Runge-Kutta algorithm to carry out the time integration. Electrons and ions share the same spatial grid (r, θ), but they have different grids in velocity space (v_r, v_θ). The semi-infinite spatial domain $[\rho \le r < \infty]$ is truncated up to a maximum radius r_{max} and discretized with N_r points. These points are not uniformly distributed, i.e., a fine grid is taken close to the probe. Thanks to the symmetry of the problem, Kilaps just simulates the range $0 \le \theta \le \pi$ using a grid of N_θ points uniformly distributed. Regarding velocity space, the infinite domains are truncated to the intervals $-v_{r_{max}} < v_r < v_{r_{max}}$ and $-v_{\theta_{max}} < v_r < v_{\theta_{max}}$. N_{v_r} and N_{v_θ} equispaced points are used to created a grid in velocity space. For convenience, we take N_{v_r} and N_{v_θ} odd numbers. Due to the disparate masses, limits of the velocity intervals are different for electrons and ions, and we set $v_{max}^{electrons} = \sqrt{\mu_i} v_{max}^{ions}$.

The total number of grid points for each specie is

$$N = N_\theta N_{v\theta}\left(N_r N_{v_r} - \frac{N_{v_r} - 1}{2}\right), \tag{6}$$

where we took into account that no grid point is necessary at $r = \rho$ and $v_r > 0$, because the distribution function is known (see Eq. (5a)). The values of the distribution function of the specie α at the grid points are organized in two vectors $\mathbf{F}^\alpha$ of dimension N ($\alpha = e, i$).

After substituting the differential operator by appropriate finite-differences formulae, Vlasov equation becomes a system of $2N$ ordinary differential equation

$$\frac{d\mathbf{F}^\alpha}{dt} = \left[\bar{\bar{M}}_L^\alpha + \frac{\epsilon_\alpha}{\mu_\alpha}\bar{\bar{M}}_{NL}^\alpha(\mathbf{F}^e, \mathbf{F}^i)\right]\mathbf{F}^\alpha + \mathbf{C}^\alpha \tag{7}$$

that we integrate with a third order Runge-Kutta method. Matrices $\bar{\bar{M}}_L^\alpha$, which have a sparse structure and only depend on the grid parameters, are computed at the beginning of the

simulation. Vectors $\mathbf{C}^{\alpha}$, which take into account the boundary conditions and the law $S(t)$, and matrices $\bar{\bar{M}}^{\alpha}_{NL}$, involving the non-linear term in Vlasov equation, are calculated each time step. Potential Φ is also found each time step by solving Poisson equation with finite-difference methods. Boundary conditions $\Phi(\rho,\theta,t)=\phi_p(t)$ and $\Phi(r_{max},\ \theta,\ t)\sim 1/r$ are imposed.

The above scheme has been parallelized in Kilaps. Each processor computes the distribution function evolution within a subdomain at certain θ value and within a radial range. In order to compute the radial and azimuthal derivatives at the boundaries of the subdomains, communication of adjacent processors each time step is needed. This strategy ensures the scalability of the code and a similar computational load to each processor.

III. EVOLUTION OF MACROSCOPIC VARIABLES

Parameter values of the simulation were $R/\lambda_{De}=0.5$, $T_e/T_i=1$, and the unrealistic mass ratio $m_i/m_e=100$. This value, which guarantees that ion motion is much slower than electron motion, helps to save computational resources. From Ref. 6, we conclude that probe radius is small enough to make the probe operate within the orbital-motion-limited (OML) regime if no probe motion would exist. The numerical parameters were $N_r=153$, $N_\theta=18$, $N_{vr}=65$, $N_{v\theta}=65$ and $r_{max}=120$ (normalized units). The limits of the simulation box in velocity space for the electrons were set to $-7.5<v_r<7.5$ and $-7.5<v_\theta<7.5$. The ion box in velocity space was scaled by a factor $\sqrt{m_e/m_i}$, and the equations were integrated with a fixed time step equal to $\Delta t=0.001\omega_{pe}^{-1}$. As shown by Sec. IV–VI, the numerical box and the resolution were large enough to impose the boundary conditions appropriately and capture the main physics of the problem. The simulation ran in 145 processor during one month, approximately. The external laws $\phi_p(t)$ and $S(t)$ were varied as shown in Fig. 1 (note the logarithmic scale in the horizontal axis).

Initially, the probe bias is zero ($\phi_p(0)=0$), the probe is at rest ($S(0)=0$), and the electron and ions distribution functions are given by Eqs. (11) and (12) in Ref. 21. The normalized potential was increased until the value $\phi_{p0}=10$, which is reached at $\omega_{pe}t\sim 20$. This part of the simulation is similar to the one performed in Ref. 21, but with a lower probe potential value. The current had an overshoot, and it approached to the OML current (per unit length) I_{OML} afterwards. We recall that I_{OML} is given by

$$I_{OML}=2eN_0R\sqrt{\frac{2e}{m_e}}\left[\sqrt{\phi_p}+\frac{1}{2}\sqrt{\frac{\pi kT_e}{e}}\exp\left(\frac{e\phi_p}{kT_e}\right)erfc\left(\frac{e\phi_p}{kT_e}\right)\right] \tag{8}$$

and corresponds to the maximum current in steady conditions of a long cylindrical Langmuir probe of radius R and bias ϕ_p operating at rest in unmagnetized, collisionless, Maxwellian plasmas of electron temperature T_e.

Probe potential was kept constant and equal to 10 in the rest of the simulation. At about $\omega_{pe}t\sim 1000$, the probe-to-plasma relative velocity was increased until it reached $S=0.5$ at $\omega_{pe}t\sim 1200$. We remark that parameter S affects the boundary conditions 5b. In the interval $1200<\omega_{pe}t<3500$, the (normalized) ram velocity is kept fixed and equal to 0.5. This is enough time to reach an state close to equilibrium. During the transient, the current dropped below I_{OML}, and then it reached an asymptotic value slightly higher than I_{OML}. The black solid line in Fig. 1 then looks thicker because the current exhibits small oscillations with frequency close to ω_{pe} (see inset in Fig. 1).

Within the interval $3500<\omega_{pe}t<4000$, S was increased from 0.5 to 1 and then kept fixed until the end of the simulation at $\omega_{pe}t\sim 7000$. Plasma response was similar to the one exhibited in the interval $1000<\omega_{pe}t<3500$; collected current decreased for a moment and it then increased up to a value slightly higher than I_{OML}. Very small oscillations in the collected current are present at the end of the simulation. A close look to the simulated variables at $\omega_{pe}t\sim 3500$ and $\omega_{pe}t\sim 7000$, including collected current, electric potential, and plasma distribution functions, indicates that the simulations were long enough to reach an state close to equilibrium. The small difference between the asymptotic collected

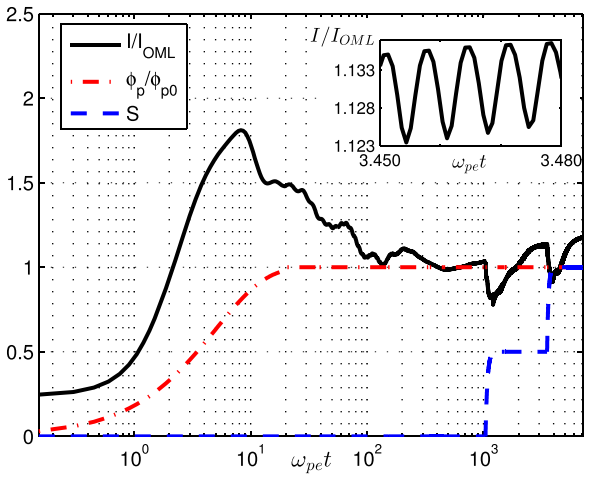

FIG. 1. Evolution of the normalized current I/I_{OML}, probe potential $\phi_p(t)/\phi_{p0}$ and probe-to-plasma relative velocity $S(t)$. Here $\phi_{p0}=10$. The inset shows the time evolution of I/I_{OML} in the interval $3450<\omega_{pe}t<3480$.

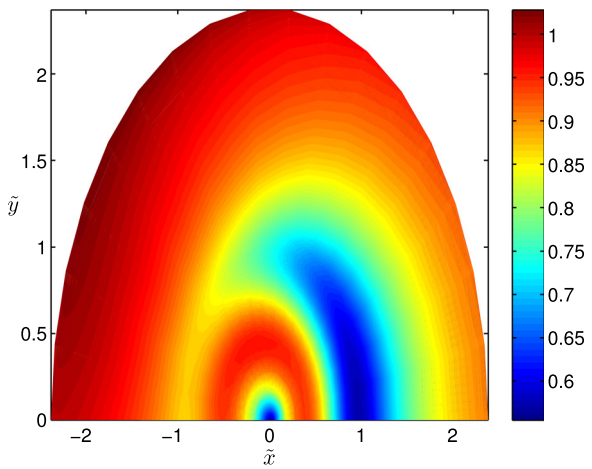

FIG. 2. Normalized electron density N_e/N_0 in log-polar coordinates at the end of a simulation ($\phi_p=10$ and $S=1$).

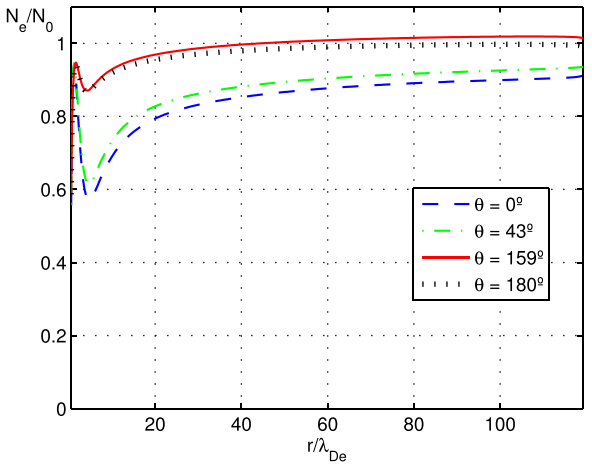

FIG. 3. Normalized electron density profiles at the end of the simulation ($\phi_p = 10$ and S = 1).

current value and I_{OML} is attributed to the slightly anisotropic character of the electron distribution function as $r \to \infty$ (note that in our simulation, we just have $\sqrt{m_i/m_e} = 10$ in Eq. (5b)).

IV. ELECTRON AND ION DENSITIES

For finite probe motion, electron density has a complex spatial structure. Figure 2 shows a map of the electron density at the end of the simulation. In order to magnify the region close to the probe, a log-polar coordinate system, with $(\tilde{x}, \tilde{y}) = \log_{10}(r/R)(\cos\theta, \sin\theta)$, is used. Very close to the probe, there is a rarified plasma with normalized electron density close to 0.5 (this is the value predicted by OML theory if no probe motion exists). As radial distance is increased, electron plasma density grows monotonically until a maximum value is reached. The maximum, about $N_e/N_0 \sim 0.94$, does not depend on the azimuthal coordinate value (see Fig. 3). Its position, however, is closer to the probe in the wake ($r/\lambda_{De} \sim 1.17$) than in the front side ($r/\lambda_{De} \sim 1.6$). For higher radial distances, the electron density decreases until a minimum value, which depends strongly on the probe side; at the front (wake), one has $N_e/N_0 \sim 0.87$ ($N_e/N_0 \sim 0.57$) at $r/\lambda_{De} \sim 4.3$ ($r/\lambda_{De} \sim 4.8$). The low electron plasma region is especially important at the wake side, within the range $2 < r/\lambda_{De} < 10$ and $0 < \theta < \pi/2$. After the minimum, the electron density grows monotonically and it approaches to the faraway value ($N_e/N_0 \to 1$). These features are in agreement with the results given by stationary-like codes.[22]

Figure 3 shows electron density profiles at certain θ angles. We recall that $\theta = 0$ ($\theta = 180°$) corresponds to the wake (front) side. There is a θ-range in the front side where the electron density is slightly above the background density within certain radial domain. For $\theta = 159°$, this radial range extends from $40\lambda_{De}$ to the border of the simulation box. This behavior, in apparent contradiction with Ref. 16, is due to a population of trapped particles and it will be analyzed in Sec. VI.

Probe-to-plasma velocity effect is illustrated in Fig. 4, which shows density profiles at the front (top panel) and wake (bottom panel) probe sides for different S values. The thick solid black lines correspond to numerical results of a stationary code (see for instance Ref. 5 or Ref. 22). The three thin lines are Kilaps results for $S = 0$, 0.5, and 1 at $\omega_{pe}t = 1000$, 3500, and 7000, i.e., once the plasma reached an equilibrium state. Clearly, the maximum in the electron density is higher for Kilaps. This is due to particle trapping (see Sec. VI), an effect not included in stationary codes. As S is increased, the maximum in the electron density decreases, and it approaches (moves away from) the probe in the wake (front) sides. Regarding the density minimum, we observe that it is less pronounced in the front side as S is enhanced but it becomes very deep in the wake side.

Figure 5 shows an ion density map at $\omega_{pe}t = 7000$. Ion density practically vanishes within the sheath, and it increases monotonically until the background plasma density N_0. The sheath has a radius about $10\lambda_{De}$, and, unlike the electron density, it exhibits a quasi-isotropic behavior. However, there is small θ-dependence, and the sheath radius is smaller in the front than in the wake side. An analysis similar to

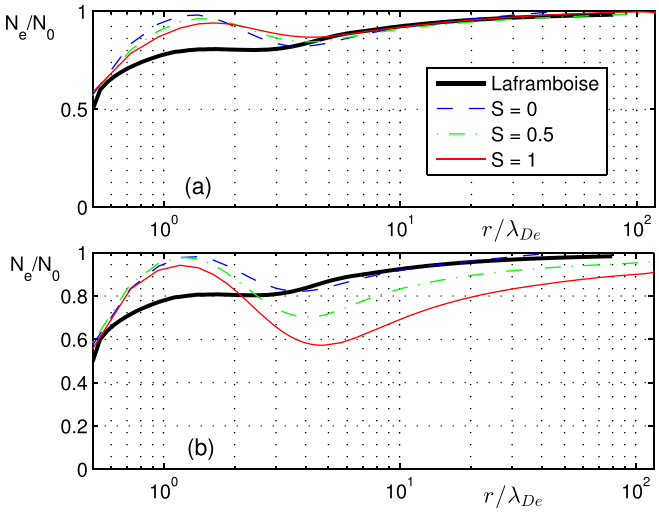

FIG. 4. Electron density at the front (top panel) and the wake (bottom panel) sides for different probe-to-plasma relative velocity. Results from Ref. 5, which ignores particle trapping, are also shown.

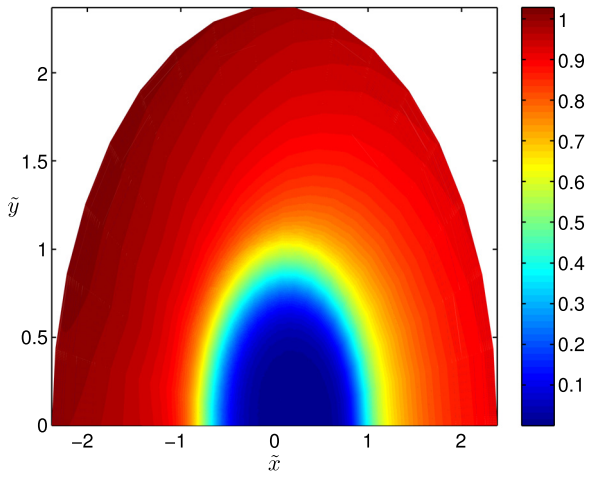

FIG. 5. Normalized ion density N_i/N_0 in log-polar coordinates at the end of the simulation.

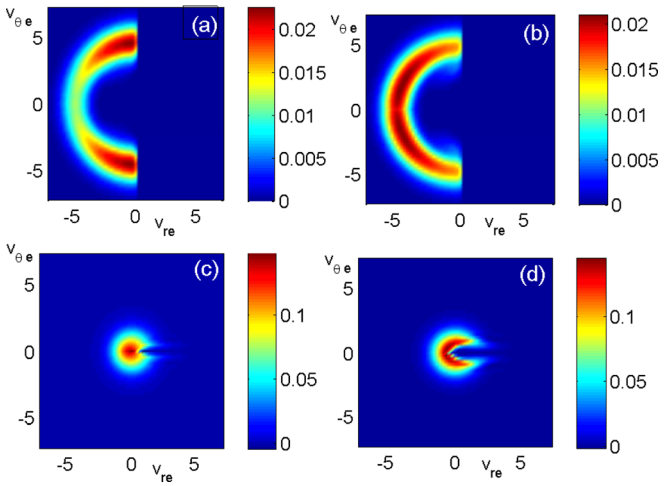

FIG. 6. Electron distribution function in velocity space at $\omega_{pe}t = 7000$. Panels (a) and (b) ((c) and (d)) correspond to sections at probe radius ($20\lambda_{De}$) and $\theta = 0°$ and $\theta = 180°$, respectively.

Fig. 4 applied to the ions (not shown) reveals that the sheath radius decreases (increases) in the front (wake) side as the parameter S in enhanced. As compared with stationary simulations, Kilaps shows that ion density in flowing plasmas is higher at the front and lower at the wake; as expected, rammed ions reach positions closer to the probe.

V. DISTRIBUTION FUNCTIONS

Electron and ion distribution functions in flowing plasmas exhibit a complex structure in real and velocity spaces. Besides a dependence on the radial and azimuthal coordinates, the distribution functions are not symmetric in velocity space (except at the specific angles $\theta = 0$ and 180°). Close to the probe, they are far from Maxwellian functions and present different features depending on the specie under consideration. Some examples are given in Figs. 6 and 7, which also show that both the computational box and the resolution in velocity space were large enough in the simulations.

Figure 6 shows the normalized electron distribution function at several positions. Panels (a) and (b) correspond to $r = \rho$ at $\theta = 0$ and $\theta = \pi$, respectively. Similarly, panels (c) and (d) display f_e at the same azimuthal angles but at $r = 20\lambda_{De}$. Panels (a) and (b) show that, at the probe radius, f_e has a shape of half a ring with a radius in velocity space of the order of $\sqrt{2e\Phi_p/m_e}$. As compared with the no-flowing case (see Fig. 3 in Ref. 21), there is a lack of electrons arriving at the probe with vanishing azimuthal velocity. This effect is important in the wake [see panel (a)] and practically negligible (but still present) in the front [panel (b)], where the electron distribution function reaches its maximum value for a normalized velocity magnitude of approximately 2. For higher radial coordinate (bottom panels), the distribution function resembles to a Maxwellian, but with vanishing number of particles at a cone that extends for positive radial velocity and has its axis at zero azimuthal velocity. The aperture angle of this cone, which is a signature of the no-emissive character of the probe, decreases as $r \to r_{max}$. At other azimuthal angles, the electron distribution functions is not symmetric with respect to the line $v_\theta = 0$; for instance, at $r = R$ and $\theta = 32°$, there are much more particles with negative azimuthal velocity (not shown).

Panels (a)–(d) in Fig. 7 display the ion distribution function at the same positions as in Fig. 6. Close to the probe, inside the sheath, the ion distribution function almost vanishes. However, due to the probe velocity, there are more ions in the front than in the wake side [see panels (a) and (b)]. As r increases, interesting and different features appear in the wake and the front sides. Panel (c) in Fig. 7 shows the ions distribution function in velocity space at $r = 20\lambda_{De}$ and $\theta = 0$ (wake). There are two peaks with centers at $v_r \sim 0.1\sqrt{kT_e/m_e}$ and $v_\theta \sim \pm 0.1\sqrt{kT_e/m_e}$. These peaks do not appear for $S = 0$ simulations, where the ion distribution function has an isotropic behavior in velocity space (except for a cone-like region with no particles due to the no emissive character of the probe).[21] Panel (d) shows the ion distribution function at the same radial distance but at the front side. Even though the probe does not emit particles, there is a prominent filament with positive radial velocity. Its azimuthal velocity range is very narrow, and it extends until $v_r \sim 0.3\sqrt{kT_e/m_e}$. This population corresponds to rammed ions that are reflected by the electric field (note that the probe is biased positively).

Figure 8 shows the structure of the filament in more detail. For convenience, we plot with a thin solid line the shifted Maxwellian distribution function given by Eq. (5b) with $S = 1$. The thick lines are ion distribution sections at $v_\theta = 0$ and $\theta = 180°$ at the end of the simulation ($\omega_{pe}t = 7000$). For $r = 2\lambda_{De}$ and $8\lambda_{De}$, the ion distribution function has a maximum at $v_r = 0$; i.e., inside the sheath, the influence of the ram motion in the ion distribution function is weak. At $r = 11\lambda_{De}$ we observe the appearance of two maxima that, as r increases, separate apart. The left peak, with $v_r < 0$, perfectly fits with the shifted Maxwellian, and it represents the incoming population of ions. The right peak, which is the filament with $v_r > 0$ in Panel (d) of Fig. 7, is a population of ions that have been reflected by the (positively polarized) probe. Although, here, we just showed the ion distribution function at the specific value $\theta = \pi$, ions are reflected in a broad θ-range. The consequence is a large

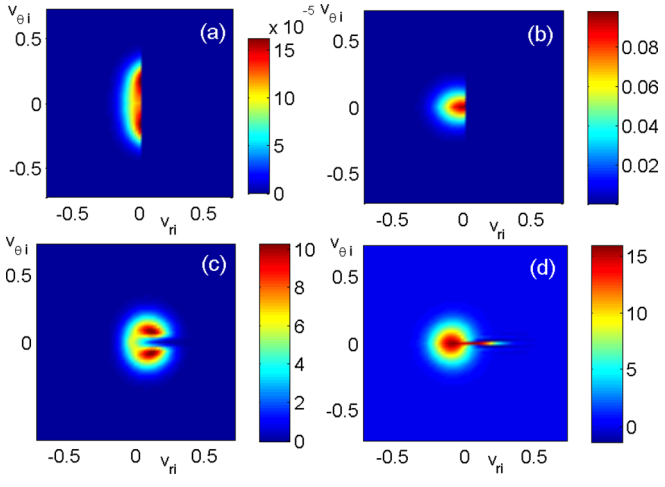

FIG. 7. Ion distribution function in velocity space at $\omega_{pe}t = 7000$. Panels (a)–(d) correspond to the same radial and azimuthal values as in Fig. 6.

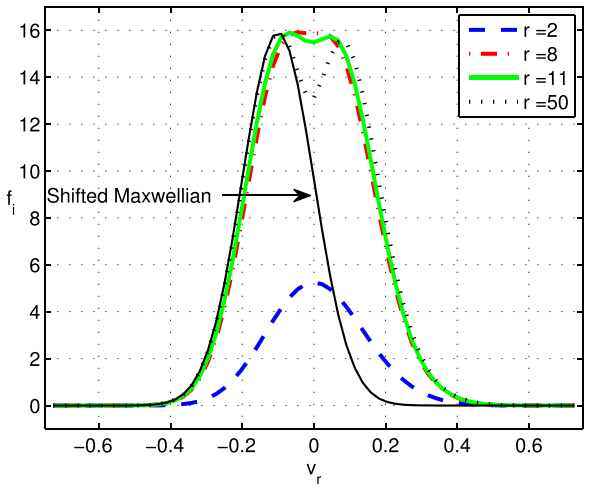

FIG. 8. The thick black line is the shifted Maxwellian given by Eq. (5b). Thin lines correspond to sections of the ion distribution function ($\theta = 180°$, $v_\theta = 0$) at $\omega_{pe}t = 7000$.

region at the probe front side with plasma density above N_0. As we will see, a trapped population of electrons is necessary to recover quasi-neutrality faraway from the probe.

VI. ELECTROSTATIC POTENTIAL AND TRAPPED PARTICLES

Figure 9 shows a map of the normalized potential (Φ/ϕ_{p0}) in log-polar coordinates at the end of the simulation. The two insets correspond to potential profiles at $\theta = \pi$ (left) and $\theta = 0$ (right). Clearly, the behavior of the potential is different at the front and wake sides of the probe. In particular, the electrostatic potential reaches negative values at the wake side, an effect already observed in stationary-like codes.[22] As we will see, the potential asymmetry has consequences in the electron trapped population, which happens at the probe front side. We remark that the potential is not stationary at the end of the simulation but exhibits small oscillations at frequency close to ω_{pe}.

Figures 3 and 4 seem to contradict results from Ref. 16; electron density close to the probe is higher in Kilaps simulations, where one also has $N_e/N_0 > 1$ in the front. As we will see, both differences are explained if trapped particles are considered. Trapped particles can be computed by post-processing Kilaps simulations. At the end of the simulation ($\omega_{pe}t = 7000$), once the plasma is in equilibrium, the (almost periodic) potential profile $\Phi(t, r, \theta)$ is saved over one electron period ($2\pi/\omega_{pe}$). Particle trajectories can then be computed by integrating Vlasov characteristic equations

$$\frac{dr}{dt} = v_r, \quad \frac{dv_r}{dt} = -\frac{\epsilon_\alpha}{\mu_\alpha}\frac{\partial \Phi}{\partial r} + \frac{v_\theta^2}{r}, \tag{9}$$

$$\frac{d\theta}{dt} = \frac{v_\theta}{r}, \quad \frac{dv_\theta}{dt} = -\frac{1}{r}\left(v_r v_\theta + \frac{\epsilon_\alpha}{\mu_\alpha}\frac{\partial \Phi}{\partial \theta}\right). \tag{10}$$

Neither the energy nor the angular momentum is conserved, because the potential depends on time and azimuthal angle θ.

Examining the electron distribution function (for instance Fig. 6), we can select initial conditions (r_0, θ_0, v_{r0}, $v_{\theta 0}$) where electrons exist at the end of the simulation. Systems 9 and 10 are integrated for a long time (typically $\omega_{pe}t \sim 50\,000$ in our calculations), and, if the particle does not hit the probe and does not leave the simulation box, then it is deemed to be trapped.

Figure 10 shows some examples of particle trajectories. Trajectory (a) corresponds to a trapped electron orbiting around the probe. This population of trapped particles is responsible for the high density (as compared with stationary theory) exhibited by Kilaps simulations close to the probe (see Fig. 4). A second population of trapped particles happens at the probe front side. An example is given by trajectory (b) in Fig. 10. Neglecting this population yields to the paradox explained in Sec. I. If it is included, one has $N_e/N_0 > 1$ at the front, and plasma can reach quasineutrality (note that $N_i/N_0 > 1$ at the front due to the reflected ions showed in Fig. 8). Finally, electrons labeled by (c) and (d) are captured by the probe and (e) goes around the probe and leaves the simulation box.

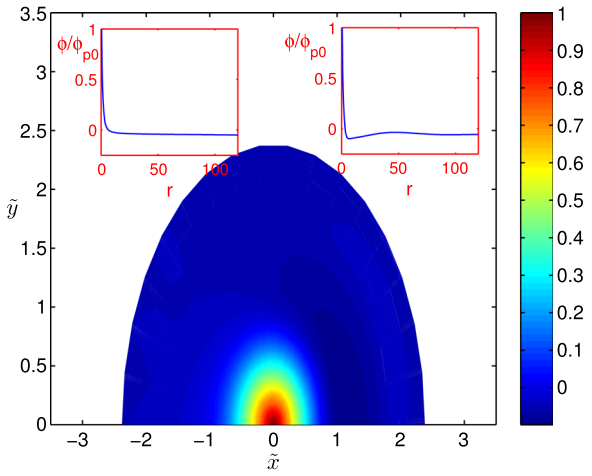

FIG. 9. Normalized electric potential Φ/Φ_{p0} in log-polar coordinates at the end of the simulation. Left (right) inset corresponds to a section at $\theta = 180°$ ($\theta = 0°$).

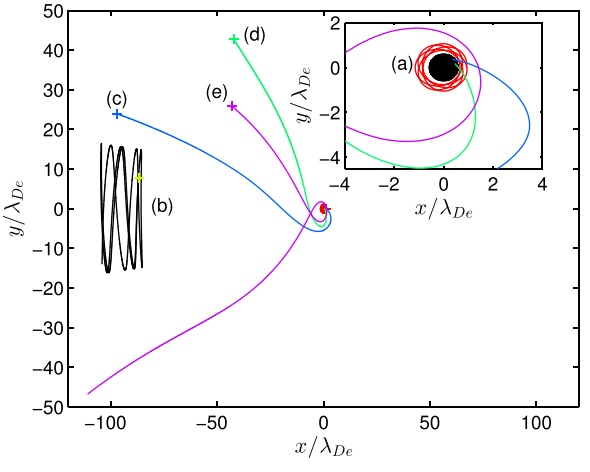

FIG. 10. Electron trajectories: (a) trapped orbit around the probe, (b) trapped orbit at the front side, (c) and (d) captured electrons and (e) trajectory leaving the simulation box. Probe, with radius $R/\lambda_{De} = 0.5$, is plotted as a black circle.

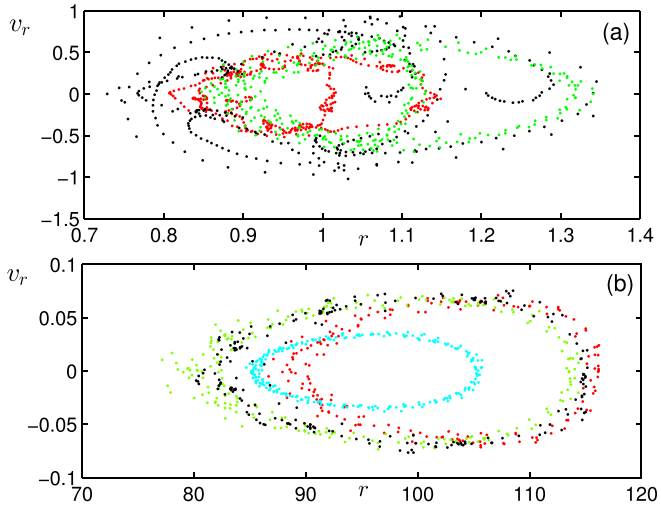

FIG. 11. Poincare sections (with the hypersurface $\theta = \pi$) of trapped electrons. Top (bottom) panel corresponds to electron orbiting around the probe (at the front).

Probe-to-plasma relative motion also produces a loss of regularity in electrons trajectories. In non-flowing plasmas and once it reached equilibrium and electric potential is time-independent, both angular momentum and energy are conserved. Systems 9 and 10 are integrable, and particle dynamics is regular. However, in flowing plasma, systems 9 and 10 are (in principle) non-integrable. This issue was investigated by plotting Poincaré sections of trapped electrons orbiting around the probe and at the front; each time an electron trajectory intersected the hypersurface $\theta = \pi$, we plotted v_r versus r. The results are shown in panels (a) and (b) of Fig. 11, where colors were used to denote trajectory started with different initial conditions. Trapped electrons trajectories are confined to certain bounded region of the phase space and exhibit a complex behavior. In the case of trapped electrons at the probe front side [panel (b)], the trajectories seem to fill tori in phase space.

VII. CONCLUSIONS

This paper presented numerical simulations of current collection by a positively polarized infinite cylinder in flowing plasmas, a problem with applications to Langmuir probes and electrodynamic tethers. The non-stationary Vlasov-Poisson solver named Kilaps was extended to incorporate the probe-to-plasma relative velocity. Since there is no longer azimuthal symmetry in flowing plasmas, the problem is very demanding from a computational point of view, and parallel computing is required. Both normalized probe bias ϕ_p and probe velocity S were varied smoothly and then kept constant during enough time to let the plasma reach an equilibrium state. Repeating this strategy for several S values allowed to make an analysis of plasma properties as a function of S.

The discretization algorithm implemented by Kilaps, an Eulerian Vlasov code, provided results free of numerical noise. However, due to the high computational cost, the dimensionless parameters used in the simulations are far from real space tether missions operating within the mesothermal regime. Since the code is parallelized, more realistic dimensionless values will be achieved in the future thanks to the development of computer clusters. This drawback did not prevent to get insight into the paradox raised in Ref. 15. The numerical simulations confirmed that particle densities exceed the background density at the probe front side (see Fig. 3), where electron trapping also occurs. This population is crucial to recover quasineutrality at the probe front and should not be neglected. A second population of electrons orbiting around the probe was also detected. Unlike the no-flowing plasma case, trapped particles trajectories do not seem to be regular and exhibit a complex behavior. We remark that neither particle energy nor angular momentum are conserved because the potential depends (periodically) on time and on the azimuthal coordinate. Another interesting footprint of the probe motion is the presence of a filament in the ion distribution function at the probe front side. This filament corresponds to rammed ions that were reflected by the probe.

Besides electron trapping, most of the feature of the simulations are in agreement with results from steady-state solvers. Electron density profiles (Figs. 2–4) are similar to the one found in Sec. 4.6.1 of Ref. 22; in the ram side, electron density minimum is less pronounced as S increases, but it becomes deeper in the wake side. A second common feature with Ref. 22 is the potential depression (below 0) on the wake side (see right inset in Fig. 9). The main difference between Kilaps simulations and the one reported in Ref. 22 is the collected current. It is slightly above I_{OML} in our simulations but decays with S in Ref. 22. Experimental measurements indicated that plasma flow leads to a current enhancement over that predicted by the OML theory.[22]

Particle trapping occurs in the simulations during the transient. It suggests that the final state of the plasma depends on the specific $S(t)$ and $\Phi_p(t)$ temporal profiles. This could be demonstrated by running two simulations with different $S(t)$ and $\phi_p(t)$ histories but equal $\phi_p(t \to \infty)$ and $S(t \to \infty)$ values. Such a calculation is beyond the scope of this paper due to computational limitations. However, the existence of multiple solutions for exactly de same value of the parameters is not new. For instance, the solution found in Ref. 21, which included particle trapping, was different to the one found in Ref. 5, and they both correspond to the same parameter values.

The parallelization scheme and the use of special subroutines to handle sparse matrices were essential to investigate Langmuir probes with Eulerian Vlasov codes. Any additional physical effect that would keep the problem within a 2-dimensional geometry, could be incorporated to the algorithm without increasing the computational cost noticeably. Some examples are the analysis of emissive Langmuir probes and the presence of an external magnetic field component along the probe axis. Extensions of Kilaps in these directions are currently in progress.

ACKNOWLEDGMENTS

The authors wish to acknowledge very helpful comments by the referee. D. Pastor-Moreno was supported by a grant from the European Commission, FP-7 Space

project BETs (No. 262972). The authors thankfully acknowledge the computer resources, technical expertise, and assistance provided by the Supercomputing and Visualization Center of Madrid (CeSViMa).

[1]H. M. Mott-Smith and I. Langmuir, "The theory of collectors in gaseous discharges," Phys. Rev. **28**, 727–763 (1926).
[2]J. R. Sanmartin, M. Martinez-Sanchez, and E. Ahedo, "Bare wire anodes for electrodynamic tethers," J. Propul. Power **9**, 353–360 (1993).
[3]I. B. Bernstein and I. N. Rabinowitz, "Theory of electrostatic probes in a low-density plasma," Phys. Fluids **2**, 112–121 (1959).
[4]S. H. Lam, "Unified theory for the Langmuir probe in a collisionless plasma," Phys. Fluids **8**, 73–87 (1965).
[5]J. G. Laframboise, "Theory of spherical and cylindrical Langmuir probes in a collisionless, Maxwellian plasma at rest," Ph.D. dissertation (University of Toronto, Canada, 1966).
[6]J. R. Sanmartín and R. D. Estes, "The orbital-motion-limited regime of cylindrical Langmuir probes," Phys. Plasmas **6**, 395–405 (1999).
[7]G. Sánchez-Arriaga and J. R. Sanmartín, "Relativistic current collection by a cylindrical Langmuir probe," Phys. Plasmas **19**, 063506 (2012).
[8]M. Kanal, "Theory of current collection of moving cylindrical probes," J. Appl. Phys. **35**, 1697–1703 (1964).
[9]W. R. Hoegy and L. E. Wharton, "Current to a moving cylindrical electrostatic probe," J. Appl. Phys. **44**(12), 5365 (1973).
[10]R. Godard and J. G. Laframboise, "Total current to cylindrical collectors in collisionless plasma flow," Planet. Space Sci. **31**, 275–283 (1983).
[11]G. Z. Xu, "The interaction of a moving spacecraft with the ionosphere: Current collection and wake structure," Ph.D. dissertation (York University, 1992).
[12]J. C. McMahon, "The interaction of infinite and finite cylindrical probes with a drifting collisionless Maxwellian plasma," Ph.D. dissertation (York University, Canada, 2000).
[13]T. Onishi, "Numerical study of current collection by an orbiting bare tether," Ph.D. dissertation (MIT, Cambridge, 2002).
[14]E. Choiniere and B. E. Gilchrist, "Self-consistent 2-D kinetic simulations of high-voltage plasma sheaths surrounding ion-attracting conductive cylinders in flowing plasmas," IEEE Trans. Plasma Sci. **35**, 7–22 (2007).
[15]J. R. Sanmartín, "Active charging control and tethers," in *CNES-Space Technology Course: Prevention of Risks Related to Spacecraft Charging*, edited by J. P. Catani (Cepadus, Toulouse, France, 2002), pp. 515–533.
[16]J. G. Laframboise and L. W. Parker, "Probe design for orbit-limited current collection," Phys. Fluids **16**, 629–636 (1973).
[17]J.-M. Siguier, P. Sarrailh, J.-F. Roussel, V. Inguimbert, G. Murat, and J. SanMartin, "Drifting plasma collection by a positive biased tether wire in LEO-like plasma conditions: Current measurement and plasma diagnostic," IEEE Trans. Plasma Sci. **41**, 3380–3386 (2013).
[18]A. V. Gurevich, "Distribution of captured particles in a potential well in the absence of collisions," Sov. J. Exp. Theor. Phys. **26**, 575 (1968).
[19]A. C. Calder and J. G. Laframboise, "Time-dependent sheath response to abrupt electrode voltage changes," Phys. Fluids B **2**, 655–666 (1990).
[20]F. Iza and J. K. Lee, "Particle-in-cell simulations of planar and cylindrical Langmuir probes: Floating potential and ion saturation current," J. Vac. Sci. Technol. A **24**, 1366–1372 (2006).
[21]G. Sánchez-Arriaga, "A direct Vlasov code to study the non-stationary current collection by a cylindrical Langmuir probe," Phys. Plasmas **20**(1), 013504 (2013).
[22]E. Choiniere, "Theory and experimental evaluation of a consistent steady-state kinetic model for two-dimensional conductive structures in ionospheric plasmas with application to bare electrodynamic tethers in space," Ph.D. dissertation (University of Michigan, 2004).